Perspective

Oxygen redox and instability in energy ceramics

Yanhao Dong[1,*] and Ju Li[2,*]

SUMMARY

Energy ceramics, including solid electrolytes and catalysts for high-temperature fuel/electrolysis cells and oxide cathodes for batteries, often experience harsh chemical and electrochemical conditions. Practical and new applications require that these devices are operated under ever more extreme redox conditions for higher energy density and power density. This challenges the stability of the energy ceramic materials and calls for a better understanding of the degradation mechanisms and innovative strategies for degradation mitigation. Here we present our analysis and perspectives on degradation phenomena in three categories of electrochemical devices of practical interest, including solid oxide fuel/electrolysis cells, protonic ceramic fuel/electrolysis cells, and lithium-ion batteries. We also discuss the stability/degradation of the key ceramic components from the view of oxygen redox and instability arising from anodic bias, transport limitation, and coupled electro-chemo-mechanics at the virtual and physical interfaces. We hope these perspectives provide design principles for electroceramic chemistry, microstructure, and processing.

INTRODUCTION

Many oxides used in energy applications are subject to harsh chemical and electrochemical conditions. For example, in solid oxide fuel/electrolysis cells[1–3] (SOFCs/SOECs, using oxygen ion as the ionic charge carrier) and protonic ceramic fuel/electrolysis cells[4–6] (PCFCs/PCECs, using proton as the ionic charge carrier), the dense solid electrolyte membrane not only separates a reducing fuel and an oxidizing air atmosphere at elevated temperatures (>600°C for SOFCs/SOECs and >400°C for PCFCs/PCECs) but also experiences electrode overpotentials that make the electrochemical conditions more extreme under electrolysis. The electrode overpotentials would further increase under the large-current-density SOEC/PCEC operations that are preferential in applications as long as the materials and device stability can be ensured. In lithium-ion batteries (LIBs), to obtain high discharge capacity and energy density, layered oxide cathodes $LiCoO_2$ and Ni-rich $LiNi_{1-x-y}Co_xMn_yO_2$ (NCM) can be charged to >4.5 V vs. Li^+/Li and Li- and Mn-rich cathodes (e.g., $xLi_2MnO_3 \cdot (1-x)$ $LiNi_{1/3}Co_{1/3}Mn_{1/3}O_2$ [LRNCM]) can be charged to 4.8 V vs. Li^+/Li, which correspond to highly oxidizing anodic conditions.[7–9] High-rate charging of LIBs and applications at low temperatures again indicate sluggish kinetics and high overpotentials. The high-voltage cathodes, if utilized in all-solid-state lithium-metal batteries, means that the solid electrolytes (e.g., garnet oxide $Li_{7-x}La_3Zr_{2-x}Ta_xO_{12}$ [LLZTO]) are subject to as reducing as <0 V vs. Li^+/Li on the anode side and as >4.5 V vs. Li^+/Li on the cathode side.[10–12] These devices and their operations pushed toward high energy/power density often result in accelerated degradations and premature failure. In this perspective, we will describe several degradation-relevant observations in energy ceramics and discuss how they can be understood from oxygen instability arising

[1]State Key Laboratory of New Ceramics and Fine Processing, School of Materials Science and Engineering, Tsinghua University, Beijing 100084, China

[2]Department of Nuclear Science and Engineering and Department of Materials Science and Engineering, Massachusetts Institute of Technology, Cambridge, MA 02139, USA

*Correspondence:
dongyanhao@tsinghua.edu.cn (Y.D.),
liju@mit.edu (J.L.)
https://doi.org/10.1016/j.xcrp.2023.101460

from anodic bias, transport limitation, and coupled electro-chemo-mechanics at the virtual and physical interfaces. They include oxygen bubble formation and electrolyte degradation in SOECs,[13–15] metallic sodium/lithium precipitation in all-solid-state batteries,[16,17] solid-on-solid bonding and catalytical reactions at the cathode-electrolyte interface in protonic ceramic cells,[18] and oxygen loss and stress corrosion cracking (SCC) in high-voltage cathodes for LIBs.[19–21] The understanding offers new guidance for better processing, novel functionality, and damage mitigation of ceramic materials and devices.

OXYGEN POTENTIAL TRANSITION AT PHYSICAL AND VIRTUAL INTERFACES IN SOLID ELECTROLYTES

To begin with, we consider a solid electrolyte device in which local equilibrium and steady-state potential distributions can be reached inside the electrolyte.[22] This should hold in SOFCs/SOECs operated at >600°C, and PCFCs/PCECs operated at >400°C, where both the major ionic charge carrier (O^{2-} or H^+) and the minor electronic charge carriers (electron and hole, both being polarons in ionic defect-rich oxide electrolytes) are quite mobile with 1 eV or smaller migration barriers. Taking yttria-stabilized zirconia (YSZ, which is the state-of-the-art electrolyte in SOFCs/SOECs) as an example and using Kröger-Vink notation, the large amount of extrinsic yttria doping introduces abundant oxygen vacancy via defect reaction

$$Y_2O_3 \ = \ 2Y'_{Zr} + V^{..}_O + 3O^{\times}_O \qquad \text{(Equation 1)}$$

The minuscule redox of YSZ electrolyte under electrochemical conditions slightly shifts the oxygen vacancy concentration via

$$O^{\times}_O \ = \ V^{..}_O + 2e + 1/2O_2 \qquad \text{(Equation 2)}$$

$$V^{..}_O + 1/2O_2 = 2h + O^{\times}_O \qquad \text{(Equation 3)}$$

For 8 mol % yttria-stabilized cubic zirconia, which is the preferred SOFC/SOEC electrolyte (Equation 1) of doping changes the chemical composition ZrO_2 to $Y_{0.148}Zr_{0.852}O_{1.926}$ with oxygen nonstoichiometry $\delta_{ex} = 0.074$. In comparison, switching the atmosphere from air with oxygen partial pressure $PO_2 = 0.21$ atm to a highly reducing one, say with $PO_2 = 10^{-20}$ atm at 800°C, only changes the oxygen nonstoichiometry by $\delta_{in} = 7.9 \times 10^{-5}$ (~0.1% of δ_{ex}) via the intrinsic reduction and oxidation reactions in Equations 2 and 3.[23,24] As a result, at a fixed temperature, the oxygen vacancy concentration and the ionic conductivity of YSZ can be viewed as a constant across the spanned PO_2 range. The PO_2 can be converted to the chemical potential of oxygen μ_{O_2} (abbreviated as oxygen potential) by the Nernst equation

$$\mu_{O_2} = \mu^{\ominus}_{O_2} + k_B T \ln(PO_2/1 \text{ atm}) \qquad \text{(Equation 4)}$$

where $\mu^{\ominus}_{O_2}$ is oxygen potential at the standard state that is set as 0 eV, k_B is the Boltzmann constant, and T is the absolute temperature in K. The fixed oxygen vacancy concentration suggests that the chemical potential of oxygen ion, $\mu_{O^{2-}}$, is also a constant. The constant ionic conductivity σ_i has been measured experimentally,[25] as shown in Figure 1A. From the law of mass action, Equations 2 and 3 give that the electron conductivity σ_e and hole conductivity σ_h follow

$$\sigma_e \ = \ \sigma_{e,0} PO_2^{-1/4} \ = \ \sigma_{e,0} \exp\left(-\mu_{O_2}/4k_B T\right) \qquad \text{(Equation 5)}$$

$$\sigma_h \ = \ \sigma_{h,0} PO_2^{1/4} \ = \ \sigma_{h,0} \exp\left(\mu_{O_2}/4k_B T\right) \qquad \text{(Equation 6)}$$

The dependencies of electron and hole conductivity on μ_{O_2} have been confirmed experimentally[25] (Figure 1A), and their sum constitutes the electronic conductivity
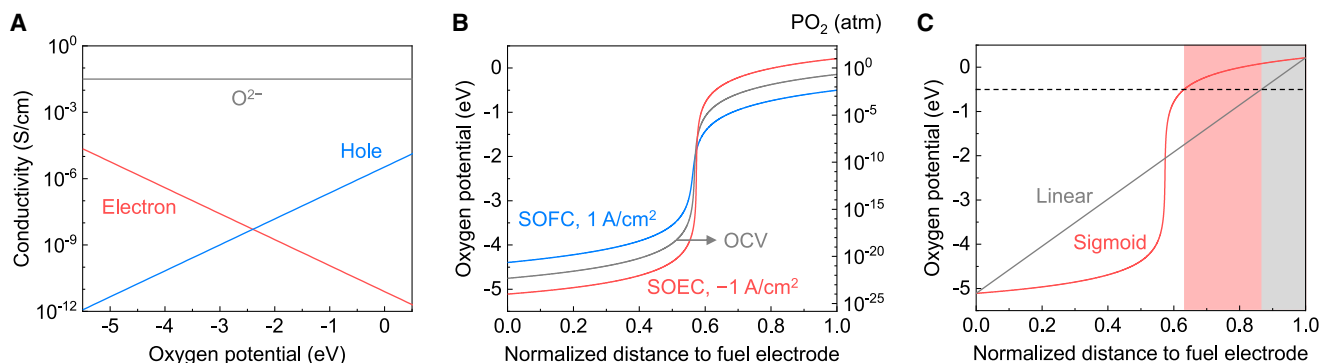
Figure 1. Conductivity and oxygen potential distributions inside solid electrolytes

(A) Conductivities of oxygen ion O^{2-}, electron, and hole in YSZ at different oxygen potentials at 800°C.

(B) Calculated spatial distribution of oxygen potential inside a 10-μm-thick YSZ electrolyte membrane under OCV (in gray), SOFC (at 1 A/cm² in blue), and SOEC (at −1 A/cm² in red) operations at 800°C. Boundary conditions of the oxygen potentials were set as −4.7531 eV at the fuel electrode/electrolyte interface and −0.1443 eV at the oxygen electrode/electrolyte interface under OCV, −4.3959 eV at the fuel electrode/electrolyte interface and −0.5015 eV at the oxygen electrode/electrolyte interface under SOFC, and −5.1103 eV at the fuel electrode/electrolyte interface and 0.2129 eV at the oxygen electrode/electrolyte interface under SOEC. Oxygen potential set as 0 eV at the standard condition of 1 atm oxygen partial pressure.

(C) Comparison of a sigmoidal and a linear oxygen potential profile. Shaded regions denote the regions with above −0.5 eV oxygen potential. Reproduced with permission from Dong et al.[26] Copyright © 2022 American Chemical Society.

σ_{eh} that has a V shape across spanned μ_{O_2} and a minimum $(\sigma_{eh})_{min} = 2\sqrt{\sigma_{e,0}\sigma_{h,0}}$. A similar defect chemistry and conductivity relationship of the major ionic and minor electronic charge carriers should hold for ceramic solid electrolytes in general. For example, conductivity data from experimental measurements are available in Gd-doped CeO_2 and Sr-/Mg-codoped $LaGaO_3$.[27,28]

The μ_{O_2} dependence of ionic and electronic conductivity has profound implications on the chemical potential and Fermi energy distributions and the degradation phenomena in solid electrolytes of the electrochemical cells.[29,26] We shall consider a one-dimensional (1D) problem for simplicity. Under the open circuit voltage (OCV) condition and steady state, the electronic leakage current driven by the Nernst potential and rate-limited by σ_{eh} needs to be constant everywhere inside the solid electrolyte. Because σ_{eh} strongly depends on local μ_{O_2}, the oxygen potential gradient $\nabla\mu_{O_2}$—which offers additional driving force for electronic charge carriers but not for ionic ones (because $\mu_{O^{2-}}$ is constant)—is not constant. $\nabla\mu_{O_2}$ is expected to be small when σ_{eh} is large and vice versa and to reach its maximum value at $(\sigma_{eh})_{min}$. Integration of such $\nabla\mu_{O_2}$ suggests a non-linear, sigmoidal μ_{O_2} profile inside the solid electrolyte as numerically shown by the gray curve in Figure 1B. The sharp oxygen potential transition halfway across the thickness direction is analogous to a "virtual interface," which separates the oxidizing half of the electrolyte on the oxygen electrode side with the reducing half of the electrolyte on the fuel electrode side. Similar sigmoidal shape also holds in SOFC and SOEC operations, as shown by the blue and red curves in Figure 1A, respectively. In addition, there are sharp oxygen potential transitions across the physical interfaces between electrodes and electrolyte, i.e., electrode overpotentials, in SOFC and SOEC operations. Because the electrode half reactions in SOFCs and SOECs take place along different directions, the boundary μ_{O_2} shift toward different directions with respect to the OCV values. The operation of SOFCs is driven by the Nernst potential, and some energy needs to be spent at the interface to drive reactions. Therefore, the boundary μ_{O_2} are less extreme than the corresponding OCV ones; i.e., μ_{O_2} at the fuel electrode/electrolyte interface is higher in SOFCs than the OCV one and μ_{O_2} at the oxygen electrode/electrolyte interface is lower in SOFCs than the OCV one. The operation of SOECs is driven

by the applied external voltage, so the boundary μ_{O_2} values are more extreme than the corresponding OCV ones, which is often quoted to explain the much faster degradation rate in SOECs compared with SOFCs. In ceria-based electrolytes, the highly reducing condition under SOEC operations (especially at higher current densities and at higher temperatures) would cause significant cation reduction from Ce^{4+} to Ce^{3+}, which increases electronic conductivity and causes internal leakage. The associated chemical expansion is also problematic.

The sharp oxygen potential transition at the virtual interface marks the transition of the dominating electronic charge carriers, from electrons (often localized at transition metal d orbitals and rare earth f orbitals) on the reducing half to holes (often localized at oxygen $2p$ orbitals) on the oxidizing half. In this sense, it can be viewed as a p-n junction. In semi-conductors, only electrons and holes are mobile. Different electron and hole concentrations in the p-type and n-type regions lead to their redistributions and the formation and depletion zone and built-in electric field at the junction. The current is electronic and the electronic conduction can be tuned by the interaction between the applied and built-in electric field. No ion conduction is involved. In the case of solid electrolytes, fast ions, electrons, and holes are mobile. The current is mostly ionic and only a minuscule part is electronic. While there is still a depletion zone of the electronic charge carriers at the virtual interface, there is no sharp electric-field variation (the electric-field magnitude is pinned by the much larger, and nearly constant, ionic conductivity) and local charge neutrality holds in the solid electrolyte.

The sigmoidal μ_{O_2} distribution translates the extreme boundary μ_{O_2} at the electrode/electrolyte interfaces to extended regions inside the solid electrolyte. As shown in Figure 1C, compared with a hypothetical linear μ_{O_2} distribution, the sigmoid one exposes most parts from the oxygen electrode/electrolyte interface to the virtual interface to a highly oxidizing condition, and similarly most parts from the fuel electrode/electrolyte interface to the virtual interface to a highly reducing condition. As a result, the degradation phenomena triggered by the extreme boundary μ_{O_2} are likely to happen not only at/near the electrode/electrolyte interfaces but also inside a significant part of the solid electrolyte. For example, high-pressure oxygen bubbles have been reported to form at the grain boundaries of YSZ electrolytes in SOEC. These bubbles are not limited to a thin region close to the oxygen electrode/electrolyte interface but extend to the region about one-half of the electrolyte thickness away from the oxygen electrode/electrolyte interface. The sharp μ_{O_2} transition at the virtual interface would further cause chemical expansion and stress concentration, as is the case for ceria-based solid electrolytes.[30] In this sense, solid electrolytes that have negligible redox activity and/or minimal chemical expansion coefficient are preferred material choices.

One of the most important electrolyte degradation mechanisms in solid oxide cells is cavitation on the oxygen electrode side, in the form of delamination of oxygen electrode from the solid electrolyte as well as the formation of isolated oxygen bubbles (early stage) and cracking (late stage) at the grain boundaries inside the solid electrolyte.[13–15] Experimental investigations show that the degradations happen in SOEC operations but not in SOFC (Figure 2), and there is an incubation time for the nucleation and growth, before which a reverse SOFC operation can mitigate the degradations in SOECs. The conventional understanding attributes the phenomena to high μ_{O_2} caused by electrode overpotential at the oxygen electrode/electrolyte interface. It is consistent with the sigmoidal μ_{O_2} distribution discussed above as the grain-boundary bubble formation and cracking indeed take place in extended regions rather than being localized at the oxygen electrode/electrolyte
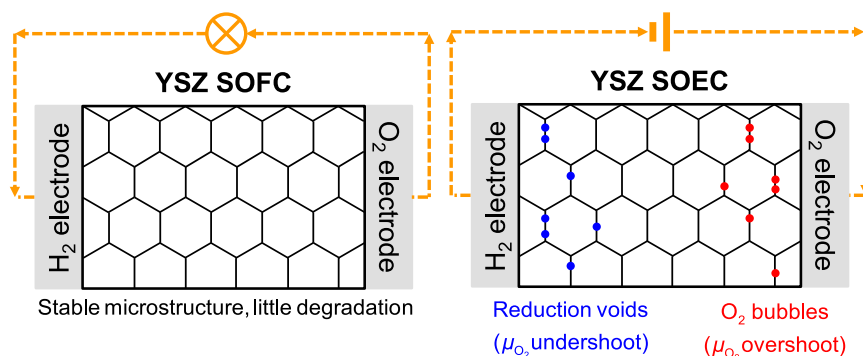
Figure 2. Schematics comparing the stability of YSZ electrolyte under SOFC and SOEC operations

Experiments show cavitation at the grain boundaries (oxygen bubbles on the oxidizing half and reduction voids on the reducing half) inside YSZ electrolyte under SOEC mode, but not SOFC. They preferential form at transverse grain boundaries (perpendicular to the electric field) but not longitudinal ones (parallel to the electric field).

interface. However, it fails to explain the preferential formation of oxygen bubbles at the transverse grain boundaries that are perpendicular to the electric-field direction, as the conventional theory predicts isotropic nucleation and growth of oxygen bubbles. This inconsistency inspired us to propose the new concept of "grain-boundary overpotential" caused by transport property mismatch (the ratio between ionic and electronic conductivity) at the grain boundaries vs. in the bulk. It is termed grain-boundary overpotential in some presentations because of its similarities to electrode overpotential: they both describe a large chemical potential change across a thin thickness and change the sign as the operation mode switches from fuel cell to electrolysis and vice versa. However, it differs from electrode overpotential as it comes from transport limitation under local equilibrium condition, while the latter is from highly irreversible reaction kinetics under non-equilibrium condition. Therefore, in the original paper,[31] we termed grain-boundary overpotential as the potential jump at grain boundaries to avoid confusion.

The grain-boundary overpotential would be best developed at transverse grain boundaries but not at longitudinal ones, thus correctly explaining the preferential nucleation and growth of oxygen bubbles observed experimentally. It also predicts potential overshoot and undershoot beyond the boundary μ_{O_2}; i.e., the most extreme electrochemical conditions can be established at the transport bottlenecks inside the solid electrolyte. In experiments, the preferential formation of oxygen bubbles at the grain boundaries away from the oxygen electrode/electrolyte interface support the proposal of μ_{O_2} overshoot. On the reducing side, the formation of reduction voids under low μ_{O_2}, and its directional preference due to μ_{O_2} undershoot has been reported in field-assisted processing of YSZ at higher current densities (up to 50 A cm^{-2}) and higher temperatures (above 1,200°C).[32] Therefore, while the critical role of electrode/electrolyte interface cannot be denied, it is equally important to properly design the microstructure and transport properties of the solid electrolytes, which has probably been overlooked in the past. While the numerical calculations[29,31,33–35] are limited to the 1D problem in oxygen ion conductors, the conceptual picture has been applied to other applications, such as all-solid-state LIBs, to guide the design of more robust materials and devices.[36,37] Potential extension of the theory is to properly treat Faradic reactions such as $O^{2-} + h = O^-$ and $O^{2-} + 2h = O^0$, which can happen and do happen inside electrolytes before stoichiometry changes and oxygen bubbles form. Some attempts have been made in our

early work,[38] which correctly predict reversible oxygen-redox activity in solid electrolytes in order to explain the experimentally observed sharp grain-size transition inside electrically loaded YSZ. It would also be worthwhile to explore the effects of $O^{2-}/O^{-}/O^{0}$ mobilities, their storage/depletion kinetics, and heterogeneous grain-boundary properties[39] in a dynamical 3D simulation.

Outside the field of solid oxide cells, metallic Na precipitates have been observed inside the bulk of beta-alumina solid electrolytes under the charging of Na-S batteries around 300°C.[16,17] These precipitates are metallic Na islands at voids, grain boundaries, and triple junctions that are not directly connected to the Na metal electrode, thus distinguishable from the often discussed Na metal dendrites. While its operation condition and redox mechanisms are different from SOFCs/SOECs, these island-type precipitates can be analogously understood from the undershoot of Na^{0} chemical potential below the standard state at internal defects inside beta-alumina solid electrolytes. Meanwhile, there is a sharp interface between the regions with and without metallic Na precipitates, in support of the discussed potential transition in YSZ electrolyte. The interface moves from Na electrode toward S electrode as the charge time progress, without an obvious increase in the amount of precipitated Na in the degraded region, again in support of the sigmoidal potential distribution.

OXYGEN ELECTRODE-ELECTROLYTE INTERFACE AND HOLE LEAKAGE IN PROTONIC CERAMIC CELLS

To cool down the operating temperature and to use cheaper materials for stacking and sealing, PCFCs/PCECs with proton-conducting solid electrolytes are under rapid development. The rationale is that H^{+} with lower absolute valence and smaller size has lower activation energy than O^{2-} and thus higher ionic conductivity at lower temperatures (e.g., 400°C–600°C). The state-of-the-art protonic ceramic electrolytes are based on perovskite $BaCeO_3$ and $BaZrO_3$ parent structure and doped with trivalent cations (e.g., Y^{3+} and Yb^{3+}), including popular compositions of $BaZr_{0.1}Ce_{0.7}Y_{0.1}Yb_{0.1}O_{3-\delta}$ (BZCYYb), $BaZr_{0.4}Ce_{0.4}Y_{0.1}Yb_{0.1}O_{3-\delta}$ (BZCYYb4411), and $BaZr_{0.8}Y_{0.2}O_{3-\delta}$ (BZY). These perovskites contain a large number of oxygen vacancies in the lattice and can be hydrated via defect reaction

$$V_O^{\cdot\cdot} + O_O^{\times} + H_2O = 2OH_O^{\cdot} \qquad \text{(Equation 7)}$$

Proton conduction is via H^{+} hopping from $OH_O^{\cdot}$ to neighboring $O_O^{\times}$. Despite the high H^{+} conductivity, there are several issues that limit the performance and applications of PCFCs/PCECs. First, the electrolytes are very difficult to densify, which requires high sintering temperature and often sintering aids (not preferred due to detrimental effects such as lowered H^{+} conductivity) as well. The sintering problem holds for half cells (including the thick hydrogen electrode support layer of hundreds of micrometers and the thin electrolyte layer of 10–20 micrometers), where the easy-to-sinter support layer consisting of NiO and electrolyte materials has already provided additional sintering force to the electrolyte layer in the co-sintering process (at T_1 above 1,400°C). Second, after co-sintering of half cells, the oxygen electrode needs to be diffusionally bonded to the surface of the dense electrolyte at relatively low temperature (T_2 around 1,000°C, to avoid coarsening of the catalysts). While a high interfacial strength between the oxygen electrode and the electrolyte is preferred, the actually obtained one is often mechanically weak and easy to detach in both cell processing and electrolysis operations. Third, while the sintered pellets of the protonic ceramic electrolytes have high H^{+} conductivity, the ones inferred by electrochemical impedance spectrum (EIS) measurements in full cells are much lower (Figure 3A) and cannot reach the intrinsic value on the materials level.[6,18,40–42]
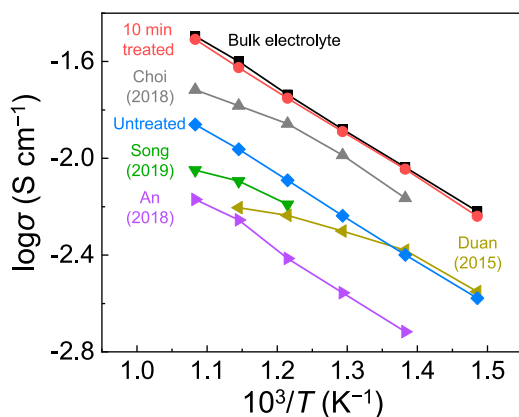
Figure 3. Calculated proton conductivity σ in bulk electrolyte and in electrochemical full cells
Data are from the literature.[6,18,40–42] Reproduced with permission from Bian et al.[18] Copyright © 2022, The Author(s), under exclusive license to Springer Nature Limited.

This causes large overpotentials, low electrochemical performance, and poor stability. Last, the protonic ceramic electrolytes have relatively high hole conductivity, especially under high-current-density PCEC operations. This lowers the Faraday efficiency of the cells and wastes energy.

Among the four major issues, we think the first three can all be attributed to the sluggish mass transport kinetics of the perovskite oxide ABO_3.[18] In perovskites, the mass transport is controlled by the slowest moving B-site cation (e.g., Zr^{4+} for $BaZrO_3$ and Ce^{4+} for $BaZrO_3$), with a rather complicated diffusion mechanism. It not only requires B-site vacancy but also needs the assistance of other ionic and electronic defects to lower the migration barrier.[43,44] Exemplified by first-principles calculations in cubic $BaTiO_3$, we showed that the B-site cation migration along the [110] direction can be assisted by A-site vacancy and electron (i.e., reduction of B-site cation) and B-site cation migration along the [100] direction can be assisted by oxygen vacancy and electron.[44] Protonic ceramic electrolytes typically contain a large number of oxygen vacancies but few A-site vacancies as A-site deficiency lowers H^+ conductivity in service. As for electronic defect, Ce has mixed valance and can be easily reduced from +4 to +3 at high temperature during sintering even in oxidizing conditions. The generated electrons can assist high-valence B-site cation migration following a polaronium mechanism, which explains why higher Ce content helps sintering of protonic ceramic electrolytes and why Ce-free BZY suffers from the most challenging sintering problem. Because of such mass transport issues, protonic ceramic electrolytes have to be co-sintered at high T_1 ($\geq 1{,}400°C$ for BZCYYb and BZCYYb4411, and $\geq 1{,}500°C$ for BZY). It makes the situation worse in the process of diffusional bonding of the oxygen electrode at T_2, as the defects at the surface of the electrolyte would be annealed away. In this sense, it would be worthwhile to explore innovative sintering cycles to decrease the sintering temperature difference $\Delta T = T_1 - T_2$ to <300°C, similar to that in SOFC/SOEC processing. This also explains the low interfacial strength of the oxygen electrode/electrolyte interface and implies limited physical contacts at the interface. In other words, the true contact area between the oxygen electrode and the electrolyte is rather low and provides few sites for interfacial reaction and proton conduction. It results in larger polarization and ohmic resistance of the cell as well as larger overpotential, which lowers device performance and stability.

Extensive efforts have been made to resolve the oxygen electrode/electrolyte interface problem. One effective method is to modify the oxygen electrode/electrolyte interface by mixed conducting oxide nanofilms. For example, dense interlayers of $PrBa_{0.5}Sr_{0.5}Co_{1.5}Fe_{0.5}O_{5+\delta}$, $La_{0.5}Sr_{0.5}CoO_{3-\delta}$, and $Ba_{0.95}La_{0.05}Fe_{0.8}Zn_{0.2}O_{3-\delta}$ with
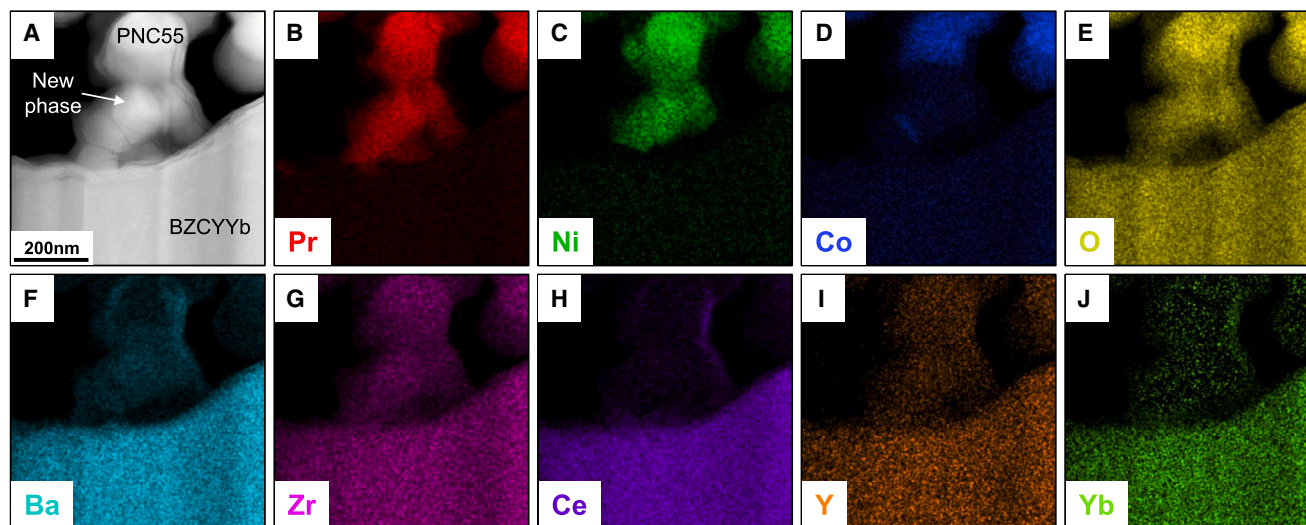
Figure 4. Reactively sintered oxygen electrode-electrolyte interface

(A–J) (A) High-angle annular dark-field scanning transmission electron microscopy image near the oxygen electrode-electrolyte interface with acid etching treatment and corresponding elemental mapping of (B) Pr, (C) Ni, (D) Co, (E) O, (F) Ba, (G) Zr, (H) Ce, (I) Y, and (J) Yb. Oxygen electrode, $PrNi_{0.5}Co_{0.5}O_{3-\delta}$. Electrolyte, BZCYYb. Reproduced with permission from Bian et al.[18] Copyright © 2022, The Author(s), under exclusive license to Springer Nature Limited.

thicknesses of a few hundred nanometers have been applied between the oxygen electrode and electrolyte to lower both the ohmic and polarization resistances of PCFCs/PCECs.[6,45–47] These perovskites are presumably triple conductors that conduct H^+, O^{2-}, and holes. We recently reported an acid etching method,[18] which was applied after the co-sintering of the half cells and before the attachment of the oxygen electrode. (Note that the acid etching process needs to be properly adjusted not to damage the bulk of electrolyte membrane. Otherwise, there could be changes in the chemical composition and crystal structure of the electrolyte that lowers proton conductivity or gas leakage issue.) Physically, it increases the roughness of the electrolyte surface. Chemically, it etches away segregated Y and Yb at the surface and creates defects such as A-site vacancy, both of which increase the surface energy and allow for better diffusional bonding. We argued that nanoscale reactive sintering takes place at the interface, as nano-grains with new perovskite phases and distinct chemical compositions have been observed between BZCYYb electrolyte and $PrNi_{0.5}Co_{0.5}O_{3-\delta}$ oxygen electrode material (Figure 4). It offers a large chemical driving force to ensure better interfacial bonding than the capillary force, thus more physical contacts between the oxygen electrode and the electrolyte and more triple phase boundaries for catalytic reactions. Despite the simplicity, our approach for the first time demonstrates intrinsic H^+ conductivity the same as the bulk value in PCFC/PCEC devices (Figure 3A). Interestingly, the acid etching treatment lowers both polarization and ohmic resistances by lowering the pre-exponential factors rather than the activation energy (Figures 5A and 5B), hence no change in the mechanisms of electrode reactions and proton conduction. This is consistent with our proposal that it is the poor contacts that limit the interfacial reaction and transport at the same time. By normalization using a dimensionless reduced temperature and a dimensionless relative resistance, we were able to collapse all the EIS data into a single master curve in an Arrhenius plot (Figure 5C), which supports a single mechanism, again consistent with the proposal. With further optimizations in the composition and microstructure of the oxygen electrode, exceptional electrochemical performance has been demonstrated in PCFC and PCEC operations.
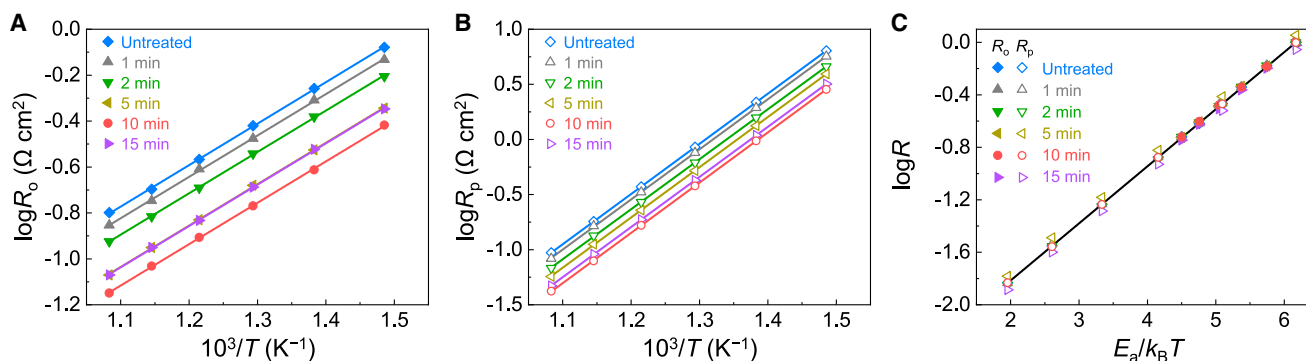
Figure 5. Analysis of improved electrochemical performance

(A and B) Arrhenius plot of (A) ohmic resistance R_o and (B) polarization resistance R_p for protonic ceramic electrochemical cells with or without acid treatment.

(C) Arrhenius plot of relative resistance R vs. the inverse of reduced temperature $k_B T / E_a$.

Reproduced with permission from Bian et al.[18] Copyright © 2022, The Author(s), under exclusive license to Springer Nature Limited.

Regarding the last issue, holes form by oxidization of the lattice oxygen ion via the defect reaction in Equation 3. Unlike reversible oxygen redox for charge storage in LIBs, such an oxidation reaction does not cause significant changes in the electrolyte composition, but dramatically increases the electronic conductivity and leakage. Compared with oxygen ion electrolytes (e.g., YSZ and GDC), the much higher hole conductivity in protonic ceramic electrolytes (e.g., BZCYYb, BZCYYb4411, and BZY) is due to higher mobility of the hole polaron.[48] It can be attributed to the perovskite crystal structure where oxygen-oxygen correlation is strong and the lattice distortion is minimal compared with the case of fluorite-structure oxides such as YSZ. The severe hole leakage problem in high-current-density PCEC is due to large anodic overpotential, which corresponds to high oxygen partial pressure in Equation 6, thus more oxidation of the lattice oxygen and higher hole concentration. (The hole mobility seems to be independent of the oxygen potential.) Obviously, more active oxygen electrode catalysts would lower the overpotential and suppress hole leakage. As the hydration reaction in Equation 7 competes with the oxidization reaction in Equation 3, high steam partial pressure would also help lower hole conductivity and suppress hole leakage. From the materials physics perspective, it is not clear whether or not high H^+ mobility and high hole mobility are always correlated with each other. It seems that they both benefit from a short oxygen-oxygen distance: H^+ hopping takes place by exchanging the positions of neighboring $OH_O^·$ and O_O^x via a bridging H^+ configuration at the saddle point of the H^+ migration event, and, similarly, hole polaron hopping takes place by exchanging the positions of neighboring $O_O^·$ and O_O^x via a bridging hole configuration at the saddle point. It is also clear whether the hole state is a large polaron or not and how its size varies with different host structure as well as dopants. Last, while Choi et al.[45] provide systematic data of proton, electron, and hole conductivity as a function of H_2O and O_2 partial pressure in BZCYYb and predicts a sigmoidal oxygen potential distribution inside BZCYYb electrolyte in electrochemical cells, such data and calculations in other systems of interest are not available and they are worth studying. These open questions need to be addressed in future research, which would guide better design of the protonic ceramic electrolytes.

CATHODE-ELECTROLYTE INTERFACE AND OXYGEN LOSS IN LIBs

The electrochemical interface between the high-voltage oxide cathodes and the liquid organic electrolytes is key to the cycling stability of LIBs. Because of the

chemical incompatibility, passivation needs to be formed between the charged cathodes (oxidizing) and the organic electrolytes (reducing). The passivation can be roughly classified into two layers. The layer closer to the electrolyte side and outside of the oxide cathode particles is called the cathode-electrolyte interphases (CEIs), which are nano-composites consisting of multiple organic and inorganic compounds. CEIs have complicated chemistry and microstructure, may not be chemically uniform across the nanoscale thickness, and could be porous[49] as well. The other layer away from the electrolyte side is formed at the surface of the charged oxide cathode particles from irreversible phase transformation, involving surface oxygen loss, reduction and short-range diffusion of transition metal ions, and cation densification. It can be called the cation-densified surface phase. For example, NiO-like rocksalt phase forms at the surface of Ni-rich layered cathodes, Co_3O_4-like spinel phase forms at the surface of high-voltage $LiCoO_2$, and Mn_3O_4-like spinel phase forms at the surface of Li- and Mn-rich layered cathodes.[50–54] The formation of passivative CEIs and cation-densified surface phase is beneficial as it widens the electrochemical stability window of the organic electrolytes in battery operation. However, their over-growth is harmful due to impedance growth, consumption of electrolytes, gassing, and other side reactions. Thin, uniform, stable passivation is preferred. In this regard, electrochemically inert oxide coatings against oxidation/delithiation have been applied to oxide cathodes to improve the high-voltage cycling stability in LIBs using both organic liquid and solid-state electrolytes. For example, $LiNbO_3$ or $Li_4Ti_5O_{12}$ nanofilms[55–57] with d^0 cations are known as good coating materials for $LiCoO_2$ and Ni-rich cathodes in all-solid-state LIBs.

The physical picture of the cathode-electrolyte interface discussed above differs from the frequently used terminology of solid electrolyte interphases (SEIs) at the anode-electrolyte interface,[58,59] in the sense that no analogy to the cation-densified surface phase can be made on the anode side. The design rules of CEIs and SEIs are similar, both being good Li^+ conductors and poor electronic conductors, thus confining the lithiation and delithiation reactions beneath the passivation and away from the electrolytes. They should also be mechanically robust and deformable at the nanoscale, as volume changes during electrochemical cycling are unavoidable except for a few rare cases. The design rules of cation-densified or artificially coated surface phase are worthy of further investigations. For example, it is not clear whether it should be a good or poor electronic conductor, as both electronically conducting and insulating cathode coatings have been shown to be beneficial for the cycling stability.[60–63]

A critical role of the cathode surface phase is to kinetically suppress the outgassing oxygen loss from the charged cathode lattice in the near-surface region. When a cathode is charged to high voltages, Li^+ and electrons are removed from the materials, creating lithium vacancies and lowering the Fermi level. The latter would eventually enter the oxygen $2p$ band, or the hybrid states with strong oxygen $2p$ characteristics. The highly delithiated cathodes are thermodynamically unstable and release oxygen if kinetics are allowed. In other words, these charged cathodes are under high oxygen potential, and a primary role of a good cathode surface phase is to kinetically suppress the short-range diffusion of labile oxygen species in the near-surface region and de-catalyze the interfacial reaction of such labile oxygen with the reducing organic electrolytes. To fundamentally address the oxygen-loss issues, we recently proposed to "store" and encapsulate labile oxygen species (from charged cathodes) in the nanoscale surface phase.[64] The proposal has been demonstrated by a perovskite surface phase with chemical composition $La_{1-w}Ca_wCoO_{3-\delta}$ artificially constructed on single-crystalline $LiCoO_2$ for high-voltage applications.
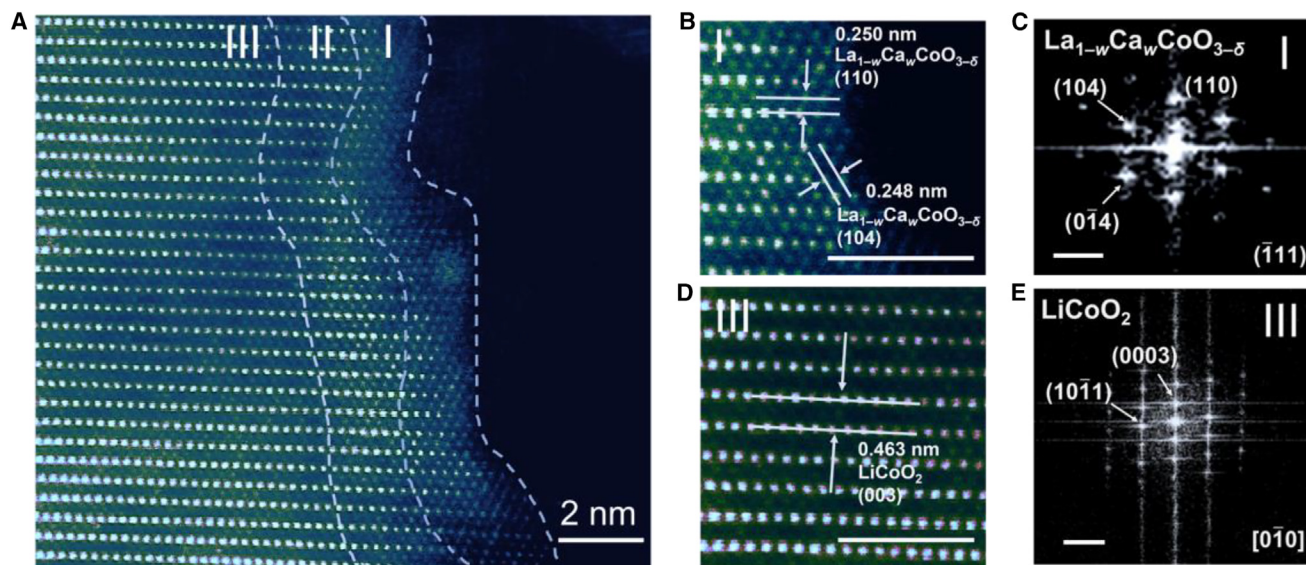
Figure 6. Lanthurized surface architecture
(A) High-angle annular dark-field scanning transmission electron microscopy image of lanthurized $LiCoO_2$ surface showing an architecture consisting of region I (perovskite surface phase), II (layered phase with La and Ca doping in the Li layer), and III (bulk $LiCoO_2$ in layered phase).
(B) Magnified image of region I and its fast Fourier transform pattern showing perovskite phase. (C) Fast Fourier transform pattern of (B).
(D) Magnified image of region III and its fast Fourier transform pattern showing layered $LiCoO_2$ phase. (F) Fast Fourier transform pattern of (D).
Scale bar, 2 nm in (B) and (D), 5 nm^{-1} in (C) and (E). Reproduced with permission from Cai et al.[64] Copyright © 2023, The Author(s), under exclusive license to Springer Nature Limited.

Via a tunable wet-chemical La^{3+}/Ca^{2+}-Li^+ ion-exchange process and heat treatment at modest temperature, high-quality conformal surface reconstruction has been achieved (Figure 6), with abundant oxygen vacancies for oxygen storage, ~8% compressive strain (with reference to the bulk $La_{1-w}Ca_wCoO_{3-\delta}$ phase) for strong O 2p-Co 3d hybridization to suppress oxygen motion, and the capability to greatly widen the anodic stability window of the cathodes. From the processing point of view, the treatment is analogous to carburizing of steel, thus termed "lanthurizing" of battery cathodes. Its applicability has also been demonstrated in Ni-rich layered cathodes and Co-free Li-/Mn-rich cathodes.

Beyond the surface, there are also oxygen instability issues in the cathode lattice and at the grain boundaries of the polycrystalline cathodes. In the former case, room-temperature long-range oxygen ion (the slowest moving species in oxide cathodes) diffusion in the lattice is not expected to be possible based on transition metal redox. This is because Fermi levels in these cathodes are away from oxygen 2p band so that oxygen ion can be treated as −2 valence, including at the saddle point during its migration. The migration barriers of O^{2-} are generally high, e.g., ~3 eV in both $LiCoO_2$ and its charged form ($Li_{0.3}CoO_2$).[20] The exceptions are so-called hybrid anion- and cation-redox (HACR) cathodes that use a large amount of reversible oxygen redox, such as LRNCM. Because Fermi levels in such cases have readily entered the oxygen 2p band, oxygen ion can dynamically change its valence and electronic structure during migration (Figure 7).[44] Of particular importance is the electronic structure relaxation at the saddle point, which lowers the energy of the supercell and thus the migration barrier. First-principles calculations in a model system[20,65] show that the migration barrier of oxygen ion can be lowered from ~3 eV in Li_2MnO_3 to less than 0.6 eV in $Li_{0.81}MnO_3$, low enough to enable long-range lattice oxygen diffusion at room temperature. This explains peculiar
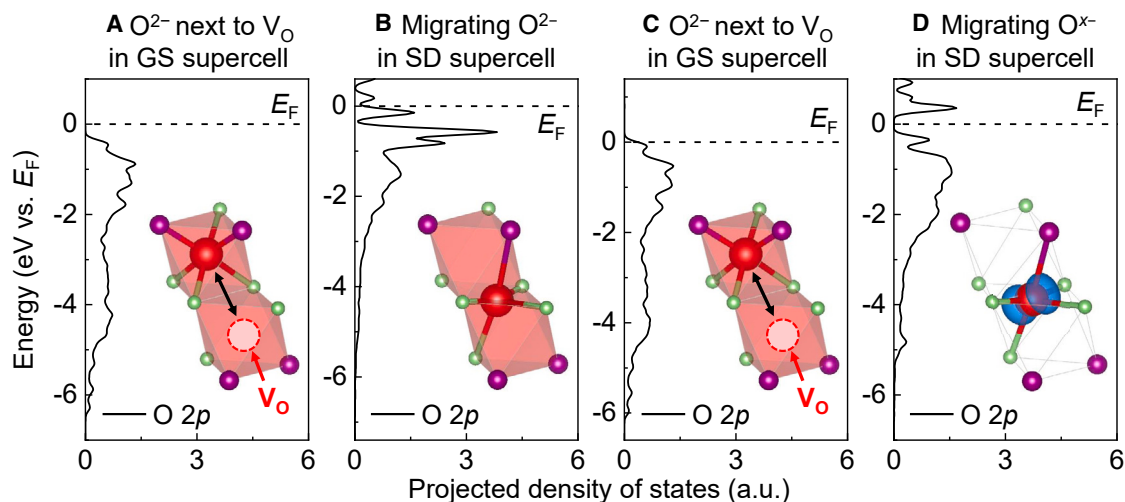
Figure 7. Electronic origin of enhanced oxygen ion mobility under oxidation

(A and B) Projected density of states of (A) a to-be-migrating O^{2-} next to an oxygen vacancy V_O in the ground state (GS) before the migration and (B) a migrating O^{2-} in the saddle point (SD) during the migration, without the extra hole.

(C and D) Projected density of states of (C) a to-be-migrating O^{x-} next to an oxygen vacancy V_O in the GS before the migration and (D) a migrating O^{x-} in the SD during the migration, with an extra hole. Insets of (A–D): schematic local structures. Inset of (D): electron cloud in blue denoting the unoccupied states (i.e., hole states) with 0.006 electron/Bohr^3 iso-charge-density. Reproduced with permission from Dong et al.[44] Copyright © 2022 Acta Materialia Inc.

experimental observations of lattice cavitation and lattice oxygen-loss-induced bulk phase transformation (e.g., from layered to spinel or rocksalt phases) in cycled LRNCM.[66]

In the latter case of polycrystalline cathodes, intergranular cracking along the grain boundaries is a major degradation mechanism.[67–69] It results in electrical insulation of the primary particles, which significantly increases the cell impedance. It generates uncoated fresh surface, which reacts with electrolytes and causes other forms of degradations. Conventional understanding attributes intergranular cracking to the anisotropic volume expansion, strain mismatch, and stress concentration, i.e., a purely mechanical event, during electrochemical cycling, which guides the development of mitigation strategies to focus on lattice doping and texture design (e.g., radially aligned grains).[70–72] However, there has been growing evidence showing that proper surface coating and electrolyte formulation could also help.[63,73–76] Based on these experimental observations, we argued that both mechanical and environmental issues should be present to cause significant intergranular cracking and proposed that it is, by definition, an SCC phenomenon[20,63,73] (Figure 8). Furthermore, if the SCC is eliminated or suppressed, there must be active plastic deformation happening at general grain boundaries during the room temperature electrochemical cycling, which requires the dynamics of oxygen ions. On the other hand, phase transformations (e.g., from layered to disordered rocksalt phases) have been reported near the un-cracked grain boundaries of Ni-rich layered cathodes after cycling, which indicates active oxygen ion diffusion along the grain boundaries at room temperature. They are probably assisted by oxygen redox and enhanced oxygen mobility as well, which implies grain-boundary oxygen ions are easier to oxidize than the lattice ones. Clearly, the stabilization of grain-boundary oxygen ions is important for the design of polycrystalline cathodes. This can be achieved by coating on the primary particle level, also known as grain-boundary infusion in the cathode literature.[60,63]
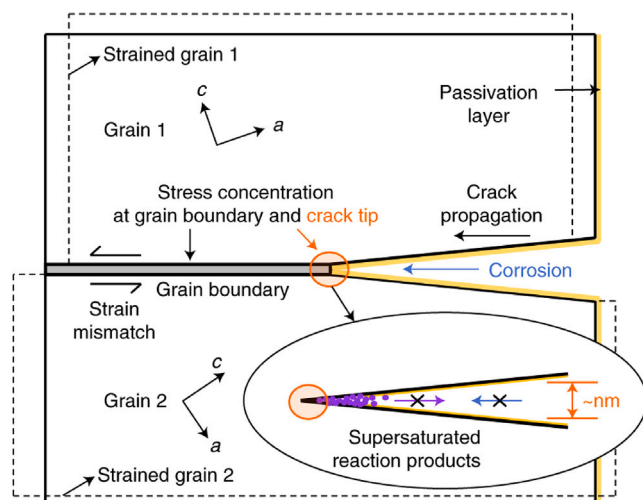
Figure 8. Schematic SCC for grain-boundary degradation in polycrystalline cathodes
Reproduced with permission from Xue et al.[73] Copyright © 2021, The Author(s), under exclusive license to Springer Nature Limited.

SUMMARY AND OUTLOOK

To summarize, oxygen instability presented here is a key issue for oxide ceramics in energy applications. Fundamental understanding of its origins, classifications, and mitigation strategies could help develop these energy materials and devices further. For SOFC/SOEC electrolytes, oxygen potential transition halfway across the thickness direction creates a virtual interface marking p-n transition in the minor electronic charge carrier and needs to be taken into account for the design of stable devices operated under harsh electrolysis conditions. Electrode overpotentials develop from interfacial reactions, which drive the boundary values of oxygen potentials toward more extreme conditions. Grain-boundary overpotentials develop from coupled transport of ionic and electronic charge carriers, which may lead to potential overshoot/undershoot in the bulk beyond the boundary value. For PCFC/PCEC electrolytes, poor solid-on-solid wetting lowers the true contact area and mechanical strength of the oxygen electrode/electrolyte interface, which decreases oxygen evolution/reduction reaction rates, limits the electrochemical performance, and shortens the life of the electrochemical cells. Acid etching and nanoscale reactive sintering at the interface have shown promise in recovering the intrinsic protonic ceramic electrolyte conductivity and activity in full cells. Hole leakage due to oxidation of lattice oxygen ions, hole polaron formation, and high mobility lowers Faraday efficiency in PCEC operations, which needs to be solved in future research. For oxide cathodes of LIBs, oxygen loss is a key issue to be addressed in high-voltage charging and extended cycling. Protections at the surface and grain boundaries, as well as the lattice in the case of oxygen-redox active cathodes, need to be properly employed to mitigate the coupled electro-chemo-mechanical interactions. Innovations in material chemistry, microstructural design, and processing techniques are clearly required to develop these energy ceramic materials further for sustainable technological applications.

ACKNOWLEDGMENTS

AUTHOR CONTRIBUTIONS

Y.D. and J.L. discussed and wrote the perspective.

DECLARATION OF INTERESTS

The authors declare no competing interests.

INCLUSION AND DIVERSITY

We support inclusive, diverse, and equitable conduct of research.

REFERENCES

1. Wachsman, E.D., and Lee, K.T. (2011). Lowering the temperature of solid oxide fuel cells. Science *334*, 935–939.

2. Hauch, A., Küngas, R., Blennow, P., Hansen, A.B., Hansen, J.B., Mathiesen, B.V., and Mogensen, M.B. (2020). Recent advances in solid oxide cell technology for electrolysis. Science *370*, eaba6118.

3. He, S., Zou, Y., Chen, K., and Jiang, S.P. (2023). A critical review of key materials and issues in solid oxide cells. Interdiscip. Mater. *2*, 111–136.

4. Yang, L., Wang, S., Blinn, K., Liu, M., Liu, Z., Cheng, Z., and Liu, M. (2009). Enhanced sulfur and coking tolerance of a mixed ion conductor for SOFCs: $BaZr_{0.1}Ce_{0.7}Y_{0.2-x}Yb_xO_{3-\delta}$. Science *326*, 126–129.

5. Duan, C., Kee, R.J., Zhu, H., Karakaya, C., Chen, Y., Ricote, S., Jarry, A., Crumlin, E.J., Hook, D., Braun, R., et al. (2018). Highly durable, coking and sulfur tolerant, fuel-flexible protonic ceramic fuel cells. Nature *557*, 217–222.

6. Choi, S., Kucharczyk, C.J., Liang, Y., Zhang, X., Takeuchi, I., Ji, H.-I., and Haile, S.M. (2018). Exceptional power density and stability at intermediate temperatures in protonic ceramic fuel cells. Nat. Energy *3*, 202–210.

7. Manthiram, A. (2020). A reflection on lithium-ion battery cathode chemistry. Nat. Commun. *11*, 1550.

8. Zhang, J.-N., Li, Q., Ouyang, C., Yu, X., Ge, M., Huang, X., Hu, E., Ma, C., Li, S., Xiao, R., et al. (2019). Trace doping of multiple elements enables stable battery cycling of $LiCoO_2$ at 4.6 V. Nat. Energy *4*, 594–603.

9. Zhang, M., Kitchaev, D.A., Lebens-Higgins, Z., Vinckeviciute, J., Zuba, M., Reeves, P.J., Grey, C.P., Whittingham, M.S., Piper, L.F.J., Van der Ven, A., and Meng, Y.S. (2022). Pushing the limit of 3d transition metal-based layered oxides that use both cation and anion redox for energy storage. Nat. Rev. Mater. *7*, 522–540.

10. Han, X., Gong, Y., Fu, K.K., He, X., Hitz, G.T., Dai, J., Pearse, A., Liu, B., Wang, H., Rubloff, G., et al. (2017). Negating interfacial impedance in garnet-based solid-state Li metal batteries. Nat. Mater. *16*, 572–579.

11. Pfenninger, R., Struzik, M., Garbayo, I., Stilp, E., and Rupp, J.L.M. (2019). A low ride on processing temperature for fast lithium conduction in garnet solid-state battery films. Nat. Energy *4*, 475–483.

12. Duan, J., Huang, L., Wang, T., Huang, Y., Fu, H., Wu, W., Luo, W., and Huang, Y. (2020). Shaping the contact between Li metal anode and solid-state electrolytes. Adv. Funct. Mater. *30*, 1908701.

13. Laguna-Bercero, M.A., Campana, R., Larrea, A., Kilner, J.A., and Orera, V.M. (2011). Electrolyte degradation in anode supported microtubular yttria stabilized zirconia-based solid oxide steam electrolysis cells at high voltages of operation. J. Power Sources *196*, 8942–8947.

14. Tietz, F., Sebold, D., Brisse, A., and Schefold, J. (2013). Degradation phenomena in a solid oxide electrolysis cell after 9000 h of operation. J. Power Sources *223*, 129–135.

15. Graves, C., Ebbesen, S.D., Jensen, S.H., Simonsen, S.B., and Mogensen, M.B. (2015). Eliminating degradation in solid oxide electrochemical cells by reversible operation. Nat. Mater. *14*, 239–244.

16. De Jonghe, L.C., Feldman, L., and Beuchele, A. (1981). Slow degradation and electron conduction in sodium/beta-aluminas. J. Mater. Sci. *16*, 780–786.

17. De Jonghe, L.C., Feldman, L., and Buechele, A. (1981). Failure modes of Na-beta alumina. Solid State Ionics *5*, 267–269.

18. Bian, W., Wu, W., Wang, B., Tang, W., Zhou, M., Jin, C., Ding, H., Fan, W., Dong, Y., Li, J., and Ding, D. (2022). Revitalizing interface in protonic ceramic cells by acid etch. Nature *604*, 479–485.

19. House, R.A., Maitra, U., Jin, L., Lozano, J.G., Somerville, J.W., Rees, N.H., Naylor, A.J., Duda, L.C., Massel, F., Chadwick, A.V., et al. (2019). Chem. Mater. *31*, 3293–3300.

20. Dong, Y., and Li, J. (2023). Oxide cathodes: functions, instabilities, self healing, and degradation mitigations. Chem. Rev. *123*, 811–833.

21. Hu, E., Yu, X., Lin, R., Bi, X., Lu, J., Bak, S., Nam, K.-W., Xin, H.L., Jaye, C., Fischer, D.A., et al. (2018). Evolution of redox couples in Li- and Mn-rich cathode materials and mitigation of voltage fade by reducing oxygen release. Nat. Energy *3*, 690–698.

22. Virkar, A.V. (2010). Mechanism of oxygen electrode delamination in solid oxide electrolyzer cells. Int. J. Hydrogen Energy *35*, 9527–9543.

23. Park, J.-H., and Blumenthal, R.N. (1989). Thermodynamic properties of nonstoichiometric yttria-stabilized zirconia at low oxygen pressures. J. Am. Ceram. Soc. *72*, 1485–1487.

24. Dong, Y., Wang, H., and Chen, I.W. (2017). Electrical and hydrogen reduction enhances kinetics in doped zirconia and ceria: I. Grain growth study. J. Am. Ceram. Soc. *100*, 876–886.

25. Park, J.-H., and Blumenthal, R.N. (1989). Electric transport in 8 mole percent Y_2O_3-ZrO_2. J. Electrochem. Soc. *136*, 2867–2876.

26. Dong, Y., Chen, I.W., and Li, J. (2022). Transverse and longitudinal degradations in ceramic solid electrolytes. Chem. Mater. *34*, 5749–5765.

27. Chatzichristodoulou, C., Chen, M., Hendriksen, P.V., Jacobsen, T., and Mogensen, M.B. (2016). Understanding degradation of solid oxide electrolysis cells through modeling of electrochemical potential profiles. Electrochim. Acta *189*, 265–282.

28. Kim, J., and Yoo, H.-I. (2001). Partial electronic conductivity and electrolytic domain of $La_{0.9}Sr_{0.1}Ga_{0.8}Mg_{0.2}O_{3-\delta}$. Solid State Ionics *140*, 105–113.

29. Jacobsen, T., and Mogensen, M. (2008). The course of oxygen partial pressure and electric potentials across an oxide electrolyte cell. ECS Trans. *13*, 259–273.

30. Marrocchelli, D., Bishop, S.R., Tuller, H.L., and Yildiz, B. (2012). Understanding chemical expansion in non-stoichiometric oxides: ceria and zirconia case studies. Adv. Funct. Mater. *22*, 1958–1965.

31. Dong, Y., Zhang, Z., Alvarez, A., and Chen, I.W. (2020). Potential jumps at transport bottlenecks cause instability of nominally ionic solid electrolytes in electrochemical cells. Acta Mater. *199*, 264–277.

32. Dong, Y., and Chen, I.W. (2018). Electrical and hydrogen reduction enhances kinetics in doped zirconia and ceria: II. Mapping electrode polarization and vacancy condensation in YSZ. J. Am. Ceram. Soc. *101*, 1058–1073.

33. Nakamura, T., Amezawa, K., Kulisch, J., Zeier, W.G., and Janek, J. (2019). Guidances for all-solid-state battery design and electrode buffer layers based on chemical potential profile calculation. ACS Appl. Mater. Interfaces *11*, 19968–19976.

34. Park, B.-K., Zhang, Q., Voorhees, P.W., and Barnett, S.A. (2019). Conditions for stable operation of solid oxide electrolysis cells: oxygen electrode effects. Energy Environ. Sci. *12*, 3053–3062.

35. Zhang, L., Zhu, L., and Virkar, A.V. (2019). Modeling of oxygen chemical potential distribution in solid oxide electrolyzer cells. J. Electrochem. Soc. 166, F1275–F1283.

36. Krauskopf, T., Richter, F.H., Zeier, W.G., and Janek, J. (2020). Physicochemical concepts of the lithium metal anode in solid-state batteries. Chem. Rev. 120, 7745–7794.

37. Wang, Y., Virkar, A.V., and Zhou, X.-D. (2021). On the thermodynamic origin of the Formation of Li-dendrites in an electrochemical cell. J. Electrochem. Soc. 168, 100503.

38. Dong, Y., and Chen, I.W. (2018). Oxygen potential transition in mixed conducting oxide electrolyte. Acta Mater. 156, 399–410.

39. Xu, X., Liu, Y., Wang, J., Isheim, D., Dravid, V.P., Phatak, C., and Haile, S.M. (2020). Variability and origins of grain boundary electric potential detected by electron holography and atom-probe tomography. Nat. Mater. 19, 887–893.

40. An, H., Lee, H.-W., Kim, B.-K., Son, J.-W., Yoon, K.J., Kim, H., Shin, D., Ji, H.-I., and Lee, J.-H. (2018). A 5×5 cm^2 protonic ceramic fuel cell with a power density of 1.3 W cm^{-2} at 600 °C. Nat. Energy 3, 870–875.

41. Duan, C., Tong, J., Shang, M., Nikodemski, S., Sanders, M., Ricote, S., Almansoori, A., and O'Hayre, R. (2015). Readily processed protonic ceramic fuel cells with high performance at low temperatures. Science 349, 1321–1326.

42. Song, Y., Chen, Y., Wang, W., Zhou, C., Zhong, Y., Yang, G., Zhou, W., Liu, M., and Shao, Z. (2019). Self-assembled triple-conducting nanocomposite as a superior protonic ceramic fuel cell cathode. Joule 3, 2842–2853.

43. Mizoguchi, T., Takahashi, N., and Lee, H.S. (2011). First-principles study on migration mechanism in SrTiO$_3$. Appl. Phys. Lett. 98, 091909.

44. Dong, Y., Qi, L., Alvarez, A., Li, J., and Chen, I.W. (2022). Enhanced mobility of cations and anions in the redox state: the polaronium mechanism. Acta Mater. 232, 117941.

45. Choi, S., Davenport, T.C., and Haile, S.M. (2018). Protonic ceramic electrochemical cells for hydrogen production and electricity generation: exceptional reversibility, stability, and demonstrated faradaic efficiency. Energy Environ. Sci. 12, 206–215.

46. Akimoto, K., Wang, N., Tang, C., Shuto, K., Jeong, S., Kitano, S., Habazaki, H., and Aoki, Y. (2022). Functionality of the cathode-electrolyte interlayer in protonic solid oxide fuel cells. ACS Appl. Energy Mater. 5, 12227–12238.

47. Tang, C., Wang, N., Zhu, R., Kitano, S., Habazaki, H., and Aoki, Y. (2022). Design of anode functional layers for protonic solid oxide electrolysis cells. J. Mater. Sci. 10, 15719–15730.

48. Kim, I.-H., Lim, D.-K., Bae, H., Bhardwaj, A., Park, J.-Y., and Song, S.-J. (2019). Determination of partial Conductivities and computational analysis of the theoretical

power density of BaZr$_{0.1}$Ce$_{0.7}$Y$_{0.1}$Yb$_{0.1}$O$_{3-\delta}$ (BZCYYb1711) electrolyte under various PCFC conditions. J. Mater. Chem. 7, 21321–21328.

49. Zhang, Z., Li, Y., Xu, R., Zhou, W., Li, Y., Oyakhire, S.T., Wu, Y., Xu, J., Wang, H., Yu, Z., et al. (2022). Capturing the swelling of solid-electrolyte interphase in lithium metal batteries. Science 375, 66–70.

50. Zou, L., Zhao, W., Jia, H., Zheng, J., Li, L., Abraham, D.P., Chen, G., Croy, J.R., Zhang, J.-G., and Wang, C. (2020). The role of secondary particle structures in surface phase transitions of Ni-rich cathodes. Chem. Mater. 32, 2884–2892.

51. Zou, L., Li, J., Liu, Z., Wang, G., Manthiram, A., and Wang, C. (2019). Lattice doping regulated interfacial reactions in cathode for enhanced cycling stability. Nat. Commun. 10, 3447.

52. Seong, W.M., Yoon, K., Lee, M.H., Jung, S.-K., and Kang, K. (2019). Unveiling the intrinsic cycle reversibility of a LiCoO$_2$ electrode at 4.8-V cutoff voltage through subtractive surface modification for lithium-ion batteries. Nano Lett. 19, 29–37.

53. Gu, M., Belharouak, I., Zheng, J., Wu, H., Xiao, J., Genc, A., Amine, K., Thevuthasan, S., Baer, D.R., Zhang, J.-G., et al. (2013). formation of the spinel phase in the layered composite cathode used in Li-ion batteries. ACS Nano 7, 760–767.

54. Oh, P., Myeong, S., Cho, W., Lee, M.-J., Ko, M., Jeong, H.Y., and Cho, J. (2014). Superior long-term energy retention and volumetric energy density for Li-rich cathode materials. Nano Lett. 14, 5965–5972.

55. Ohta, N., Takada, K., Sakaguchi, I., Zhang, L., Ma, R., Fukuda, K., Osada, M., and Sasaki, T. (2007). LiNbO$_3$-Coated LiCoO$_2$ as cathode material for all solid-state lithium secondary batteries. Electrochem. Commun. 9, 1486–1490.

56. Li, X., Jin, L., Song, D., Zhang, H., Shi, X., Wang, Z., Zhang, L., and Zhu, L. (2020). LiNbO$_3$-Coated LiNi$_{0.8}$Co$_{0.1}$Mn$_{0.1}$O$_2$ cathode with high discharge capacity and rate performance for all-solid-state lithium battery. J. Energy Chem. 40, 39–45.

57. Ohta, N., Takada, K., Zhang, L., Ma, R., Osada, M., and Sasaki, T. (2006). Enhancement of the high-rate capability of solid-state lithium batteries by nanoscale interfacial modification. Adv. Mater. 18, 2226–2229.

58. Peled, E. (1979). The electrochemical behavior of alkali and alkaline earth metals in nonaqueous battery systems—the solid electrolyte interphase model. J. Electrochem. Soc. 126, 2047–2051.

59. Peled, E., and Menkin, S. (2017). Review—SEI: past, present and future. J. Electrochem. Soc. 164, A1703–A1719.

60. Yan, P., Zheng, J., Liu, J., Wang, B., Cheng, X., Zhang, Y., Sun, X., Wang, C., and Zhang, J.-G. (2018). Tailoring grain boundary structures and chemistry of Ni-rich layered cathodes for enhanced cycle stability of lithium-ion batteries. Nat. Energy 3, 600–605.

61. Zhang, X., Belharouak, I., Li, L., Lei, Y., Elam, J.W., Nie, A., Chen, X., Yassar, R.S., and Axelbaum, R.L. (2013). Structural and electrochemical study of Al$_2$O$_3$ and TiO$_2$ coated Li$_{1.2}$Ni$_{0.13}$Mn$_{0.54}$Co$_{0.13}$O$_2$ cathode material using ALD. Adv. Energy Mater. 3, 1299–1307.

62. Li, X., Liu, J., Banis, M.N., Lushington, A., Li, R., Cai, M., and Sun, X. (2014). Atomic layer deposition of solid-state electrolyte coated cathode materials with superior high-voltage cycling behavior for lithium-ion battery application. Energy Environ. Sci. 7, 768–778.

63. Yoon, M., Dong, Y., Hwang, J., Sung, J., Cha, H., Ahn, K., Huang, Y., Kang, S.J., Li, J., and Cho, J. (2021). Reactive boride infusion stabilizes Ni-rich cathodes for lithium-ion batteries. Nat. Energy 6, 362–371.

64. Cai, M., Dong, Y., Xie, M., Dong, W., Dong, C., Dai, P., Zhang, H., Wang, X., Sun, X., Zhang, S., et al. (2023). Stalling oxygen evolution in high-voltage cathodes by lanthurization. Nat. Energy 8, 159–168.

65. Lee, E., and Persson, K.A. (2014). Structural and chemical evolution of the layered Li-excess Li$_x$MnO$_3$ as a function of Li content from first-principles calculations. Adv. Energy Mater. 4, 1400498.

66. Yan, P., Zheng, J., Tang, Z.-K., Devaraj, A., Chen, G., Amine, K., Zhang, J.-G., Liu, L.-M., and Wang, C. (2019). Injection of oxygen vacancies in the bulk lattice of layered cathodes. Nat. Nanotechnol. 14, 602–608.

67. Liu, H., Wolfman, M., Karki, K., Yu, Y.-S., Stach, E.A., Cabana, J., Chapman, K.W., and Chupas, P.J. (2017). Intergranular cracking as a major cause of long-term capacity fading of layered cathodes. Nano Lett. 17, 3452–3457.

68. Yan, P., Zheng, J., Chen, T., Luo, L., Jiang, Y., Wang, K., Sui, M., Zhang, J.-G., Zhang, S., and Wang, C. (2018). Coupling of electrochemically triggered thermal and mechanical effects to aggravate failure in a layered cathode. Nat. Commun. 9, 2437.

69. Sun, H.-H., and Manthiram, A. (2017). Impact of microcrack generation and surface degradation on a nickel-rich layered Li[Ni$_{0.9}$Co$_{0.05}$Mn$_{0.05}$]O$_2$ cathode for lithium-ion batteries. Chem. Mater. 29, 8486–8493.

70. Sun, Y.-K., Chen, Z., Noh, H.-J., Lee, D.-J., Jung, H.-G., Ren, Y., Wang, S., Yoon, C.S., Myung, S.-T., and Amine, K. (2012). Nanostructured high-energy cathode materials for advanced lithium batteries. Nat. Mater. 11, 942–947.

71. Xu, Z., Jiang, Z., Kuai, C., Xu, R., Qin, C., Zhang, Y., Rahman, M.M., Wei, C., Nordlund, D., Sun, C.-J., et al. (2020). Charge distribution guided by grain crystallographic orientations in polycrystalline battery materials. Nat. Commun. 11, 83.

72. Kim, U.-H., Park, G.-T., Son, B.-K., Nam, G.W., Liu, J., Kuo, L.-Y., Kaghazchi, P., Yoon, C.S., and Sun, Y.-K. (2020). Heuristic solution for

achieving long-term cycle stability for Ni-rich layered cathodes at full depth of discharge. Nat. Energy 5, 860–869.

73. Xue, W., Huang, M., Li, Y., Zhu, Y.G., Gao, R., Xiao, X., Zhang, W., Li, S., Xu, G., Yu, Y., et al. (2021). Ultra-high-voltage Ni-rich layered cathodes in practical Li metal batteries enabled by a sulfonamide based electrolyte. Nat. Energy 6, 495–505.

74. Li, W., Dolocan, A., Li, J., Xie, Q., and Manthiram, A. (2019). Ethylene carbonate-free electrolytes for high-nickel layered oxide cathodes in lithium-ion batteries. Adv. Energy Mater. 9, 1901152.

75. Kim, J., Lee, J., Ma, H., Jeong, H.Y., Cha, H., Lee, H., Yoo, Y., Park, M., and Cho, J. (2018). Controllable solid electrolyte interphase in nickel-rich cathodes by an electrochemical

rearrangement for stable lithium-ion batteries. Adv. Mater. 30, 1704309.

76. Xu, G.-L., Liu, Q., Lau, K.K.S., Liu, Y., Liu, X., Gao, H., Zhou, X., Zhuang, M., Ren, Y., Li, J., et al. (2019). Building ultraconformal protective layers on both secondary and primary particles of layered lithium transition metal oxide cathodes. Nat. Energy 4, 484–494.